



A Tidally Induced Global Corrugation Pattern in an External Disk Galaxy Similar to the Milky Way

Facundo A. Gómez^{1,2} , Sergio Torres-Flores^{1,2}, Catalina Mora-Urrejola², Antonela Monachesi^{1,2} , Simon D. M. White³, Nicolas P. Maffione^{4,5}, Robert J. J. Grand³ , Federico Marinacci⁶ , Rüdiger Pakmor³ , Volker Springel³ , Carlos S. Frenk⁷ , Philippe Amram⁸, Benoît Epinat⁸, and Claudia Mendes de Oliveira⁹

¹ Instituto de Investigación Multidisciplinar en Ciencia y Tecnología, Universidad de La Serena, Raúl Bitrán 1305, La Serena, Chile

² Departamento de Astronomía, Universidad de La Serena, Av. Juan Cisternas 1200 Norte, La Serena, Chile

³ Max-Planck-Institut für Astrophysik, Karl-Schwarzschild-Str. 1, D-85748 Garching, Germany

⁴ Universidad Nacional de Río Negro, Río Negro, Argentina

⁵ Consejo Nacional de Investigaciones Científicas y Técnicas, Argentina

⁶ Department of Physics & Astronomy, University of Bologna, via Gobetti 93/2, I-40129 Bologna, Italy

⁷ Institute for Computational Cosmology, Department of Physics, University of Durham, South Road, Durham DH1 3LE, UK

⁸ Aix Marseille Univ, CNRS, CNES, LAM, Marseille, France

⁹ Departamento de Astronomia, Instituto de Astronomia, Geofísica e Ciências Atmosféricas da USP, Cidade Universitaria, CEP: 05508-900, São Paulo, SP, Brazil

Received 2020 August 10; revised 2020 November 16; accepted 2020 November 23; published 2021 February 9

Abstract

We study the two-dimensional (2D) line-of-sight velocity (V_{los}) field of the low-inclination, late-type galaxy VV304a. The resulting 2D kinematic map reveals a global, coherent, and extended perturbation that is likely associated with a recent interaction with the massive companion VV304b. We use multiband imaging and a suite of test-particle simulations to quantify the plausible strength of in-plane flows due to nonaxisymmetric perturbations and show that the observed velocity flows are much too large to be driven either by a spiral structure or by a bar. We use fully cosmological hydrodynamical simulations to characterize the contribution from in- and off-plane velocity flows to the V_{los} field of recently interacting galaxy pairs like the VV304 system. We show that, for recently perturbed low-inclination galactic disks, the structure of the residual velocity field, after subtraction of an axisymmetric rotation model, can be dominated by vertical flows. Our results indicate that the V_{los} perturbations in VV304a are consistent with a corrugation pattern. Its V_{los} map suggests the presence of a structure similar to the Monoceros ring seen in the Milky Way. Our study highlights the possibility of addressing important questions regarding the nature and origin of vertical perturbations by measuring the line-of-sight velocities in low-inclination nearby galaxies.

Unified Astronomy Thesaurus concepts: Galaxy stellar disks (1594); Disk galaxies (391); Galaxy dynamics (591); Galaxy kinematics (602)

1. Introduction

Over the last decade a significant number of observational studies have provided strong evidence of an oscillating vertical asymmetry in our own Galactic disk (e.g., Widrow et al. 2012; Xu et al. 2015). Well-known features observed in the Milky Way, such as the Monoceros Ring (Newberg et al. 2002; Yanny et al. 2003), the TriAnd clouds (Price-Whelan et al. 2015), and the recently discovered A13 overdensity (Sheffield et al. 2018), can be naturally accounted for by this asymmetry, best described as a corrugation pattern (Laporte et al. 2018b). With the recent arrival of Gaia Data Release 2 (Gaia Collaboration et al. 2018), we have had direct confirmation that our own Galactic disk is undergoing phase mixing of a nonequilibrium perturbation (Antoja et al. 2018). Most successful models to describe the origin of this perturbation rely on the interaction between the Galaxy and the Sagittarius dwarf spheroidal galaxy, together with a recent boost from the Magellanic Clouds system (e.g., Gómez et al. 2012, 2013; Laporte et al. 2018a, 2018b, 2019; Bland-Hawthorn et al. 2019).

A corrugation pattern is manifested by an extended and oscillatory vertical displacement of the disk with respect to the overall disk midplane. Studies that have assessed the frequency with which corrugation patterns arise in late-type galaxies, based on cosmological simulations, have shown that such

patterns are expected to be common (Gómez et al. 2016, 2017). Large observational samples of nearly edge-on disk galaxies have revealed that $\sim 70\%$ show a perturbed vertical structure (e.g., Reshetnikov & Combes 1998; Ann & Park 2006), typically displaying S-shaped warps. However, evidence for more complex corrugation patterns in external galaxies is still extremely limited (Fridman et al. 1998; Alfaro et al. 2001; Sánchez-Gil et al. 2015), and no full two-dimensional (2D) maps of coherent and global features, similar to those observed in the Milky Way, have been reported. Morphological signatures of these vertical perturbations in external galaxies are washed out due to projection effects, independently of the inclination of the galactic disk. Thus, they cannot be detected through classical imaging. Instead, thanks to the expected 90° difference in oscillation phase between the local disk's mean height, $\langle Z \rangle$, and mean vertical velocity, $\langle V_Z \rangle$ (e.g., Gómez et al. 2013), a corrugation pattern can be revealed through line-of-sight velocity fields, V_{los} , of low-inclination disks (e.g., Gómez et al. 2017). In traditional long-lit spectroscopic observations, such patterns can be easily confused with the effects of local perturbations such as fountain flows (Sánchez-Gil et al. 2015). Therefore, full 2D kinematic maps are preferable to search for global and coherent patterns. Low-inclination angles are also required to avoid significant contamination from in-plane flows in the resulting V_{los} maps (e.g., Grand et al. 2016b).

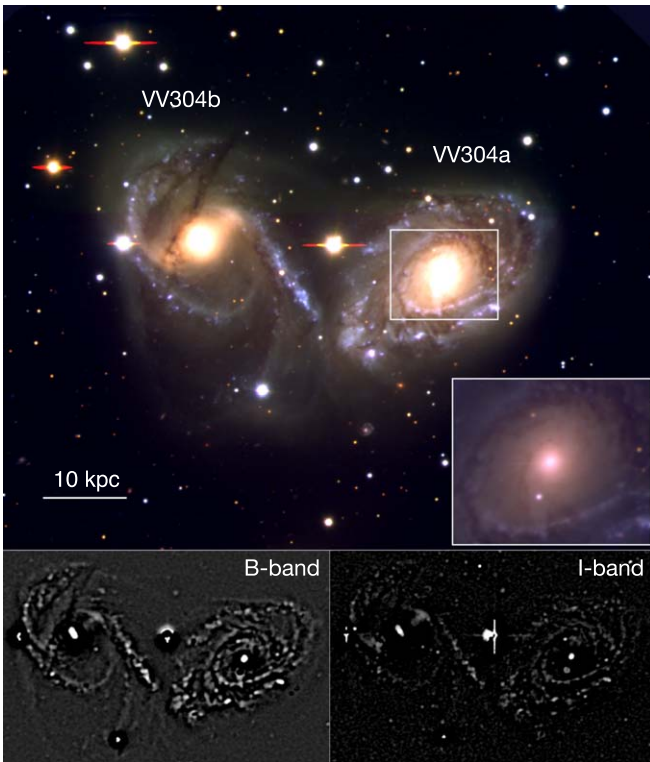


Figure 1. Top panel: optical image of the interacting pair VV304. Both galaxies show clear indications of recent interaction. The u' , g' , and r' -band false color image was obtained with the GMOS instrument at the Gemini South Observatory, under the scientific program GS-2013B-Q-27. Blue, green, and red colors are associated with each of the three filters. The inset (white square) allows visual inspection of the inner galactic regions in significantly more detail. Note that, unlike VV304b, VV304a does not possess a well-defined bar. Bottom panel: the left and right panels show structure maps in the B- and I-band, respectively, obtained from the publicly available database of the The Carnegie–Irvine Galaxy Survey.¹⁰ These maps clearly show the absence of a strong bar and the lack of a dominant bisymmetric spiral structure in the galaxy VV304a. Note as well the strongly double-barred nature of VV304b.

Here, we present a full 2D kinematic map of a Milky Way-type galaxy, namely VV304a, that shows a global, coherent and extended perturbation consistent with a corrugation pattern, likely associated with the recent interaction with its massive companion, VV304b.

2. The Perturbed Velocity Field of VV304a

2.1. VV304a: General Properties

VV304a is a late-type galaxy that has recently interacted with its closest companion, VV304b (Torres-Flores et al. 2014, hereafter TF14). VV304a is located at a distance of ~ 54 Mpc, has an optical radius of $R_{\text{opt}} \approx 18$ kpc, and a rotational-velocity curve that peaks at ~ 245 km s $^{-1}$ (TF14). Based on the observed circular velocity profile, obtained using H_{α} Fabry–Perot observations (see Section 2.2), TF14 estimated a total VV304a dynamical mass within R_{opt} of $M(< R_{\text{opt}}) \approx 2.5 \times 10^{11} M_{\odot}$. These broad properties are similar to those of the Milky Way (Liu et al. 2017; McMillan 2017; Cautun et al. 2020). Its companion, VV304b, also a late-type galaxy, has an optical radius of 18 kpc and a peak circular rotational velocity of ~ 200 km s $^{-1}$. The top panel of Figure 1 shows a u' , g' , and r' -band Gemini/Gemini Multi-Object Spectrograph (GMOS) false color image of the VV304 pair. The pair show clear signatures of recent



Figure 2. Multiband image of the VV304 galactic pair, with isophotal contours. This image contains observations from WISE 22 microns (red), FUV GALEX (1530 Å, blue), and the r' -band optical image (Gemini/GMOS, green). The isophotes were derived from the r' -band image.

interaction, which makes VV304a an ideal candidate to search for a corrugated vertical structure. Visual inspection of this panel reveals that, unlike VV304b which shows a clear double-barred structure and well-defined grand design spiral arms, VV304a does not possess any clear strong $m = 2$ perturbation. This is particularly relevant for our study since strong $m = 2$ modes could drive large in-plane velocity flows that could contribute significantly to, or even dominate, perturbations in the V_{los} field of VV304a.

To better characterize the morphological structure of VV304a, we show, on the left and right bottom panels of Figure 1, structure maps in the B- and I-band, respectively. Structure maps, originally developed by Pogge & Martini (2002), are a powerful method to enhance fine structural features in single-filter images. The maps were obtained from the publicly available database of the The Carnegie–Irvine Galaxy Survey¹⁰, and presented by Ho et al. (2011). The structure maps obtained in both filters clearly show the absence of a strong bar in VV304a. In addition, they also highlight the lack of a dominant bisymmetric spiral structure. Interestingly, one can clearly see the strongly double-barred nature of VV304b, demonstrating the strength of this method.

In Figure 2 we show a multiband image of the VV304 galactic pair. To create this image we have used observations from:

1. Red: Wide-field Infrared Survey Explorer (WISE) 22 microns. Heated dust by UV photons.
2. Blue: far-UV Galaxy Evolution Explorer (1530 Å). UV photons associated with massive (young) stars.
3. Green: r' -band optical image (Gemini/GMOS). Reddest optical band we have available.

The lack of any strong bar in the inner regions of VV304a is also evident from this image. The isocontour curves highlight the very round shape of the inner regions, only distorted by the presence of a foreground star. In the outer regions, the isocontours are distorted, reflecting the recent tidal interaction with VV304b.

2.2. H_{α} Fabry–Perot Observations

In this work we analyze the 2D kinematic field of VV304a’s H_{α} distribution, obtained from Fabry–Perot observations

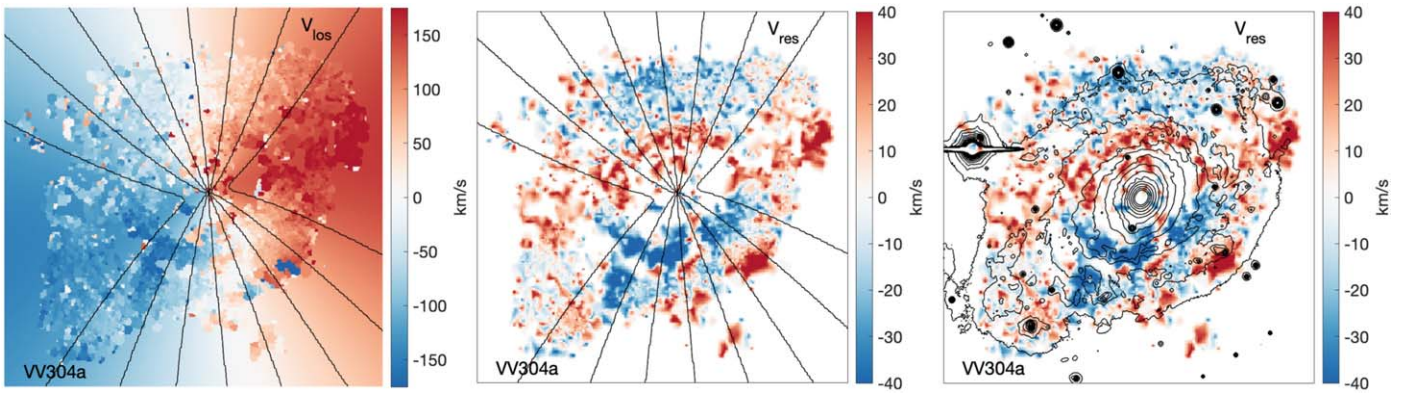


Figure 3. Left panel: observed line-of-sight velocity field, V_{los} , of VV304a, derived from its H_{α} emission. The smooth colored background shows the modeled axisymmetric velocity field in regions without observable H_{α} . The black lines show isovelocity contours of this axisymmetric field. Middle panel: residual velocity field, V_{res} , obtained from the difference between the observed and modeled V_{los} field. The transitions from positive to negative velocities along a given isovelocity line are consistent with a corrugation pattern. These velocity fluctuations could indicate a significant displacement of the disk’s $\langle Z \rangle$ with respect to its overall midplane. Right panel: residual velocity field including isophotal contours obtained from r' -band optical image (Gemini/GMOS).

published by TF14. The data were obtained with the instrument CInématique des GALaxiEs (CIGALE) mounted on the European Southern Observatory’s 3.6 m telescope at La Silla (Chile). These types of observations are ideal for deriving 2D kinematic maps due to their large field of view (207×207 arcsec²), high spectral resolution ($R \sim 13000$), and signal-to-noise ratios ($S/N \sim 5$). The data reduction process has been extensively described in TF14. Here we summarize the main steps taken to derive the 2D velocity fields.

The H_{α} 3D data cube of VV304a was reduced using a publicly available package, which is described in detail in Daigle et al. (2006).¹¹ The package provides the velocity moment maps of the H_{α} 3D data cube and it has been used by different authors during the last few years (e.g., Boselli et al. 2018; Muñoz-Elgueta et al. 2018; Gómez-López et al. 2019). The main advantage of the techniques implemented in this package is the use of adaptive spatial binning, based on a 2D Voronoi tessellation method, applied to the spatial dimensions of the 3D data cubes. As a result, it allows one to obtain high spatial resolution in high S/N regions and large spatial coverage in low S/N regions. Here we demanded a uniform S/N over the whole field of view. This was achieved by binning neighboring pixels, until a signal-to-noise target (S/Nt) is reached. For each bin, the noise is determined from the ratio between the H_{α} line flux and the rms of the continuum. Note that regions of initial S/N higher than S/Nt are not binned, thus keeping the angular resolution as high as possible. In this work, $S/Nt = 6$ was used. To remove the OH sky lines, the reduction process of the Fabry–Perot data produces a sky cube, which is removed from the observed cube. In practice, the sky cube is derived from sky-dominated regions as follows. Considering that the H_{α} emission line of a galaxy displays small shifts in frequency due to the rotation of the gas, the sky emission lines correspond to the ones that always appear in the same frequency across the cube. Based on this, the reduction process applies a spatial binning on the data cube, in order to reach a desired S/N on the sky lines. At the same time it creates a median spectrum of the cube. A cross correlation between the median spectrum and the spatially-binned sky regions allow us

to determine the sky-dominated regions, which are used to produce a sky cube. Finally, the sky cube is subtracted from the original observed data cube. We refer the reader to TF14 for more details.

2.3. VV304a Residual V_{los} Field

In the top panel of Figure 3 we show the V_{los} field of VV304a, derived from the H_{α} data cube. Note that H_{α} emission in this galaxy can be detected up to its optical radius (see Figure B1 of TF14). Thus it can be used to map the kinematics of the disk’s outskirts. The kinematic position angle $PA = 104^{\circ} \pm 2^{\circ}$, inclination angle $i = 39^{\circ} \pm 12^{\circ}$, systemic velocity $V_{\text{sys}} = 3811 \pm 3 \text{ km s}^{-1}$, and rotation curve were estimated by fitting an axisymmetric velocity field model to the observed data and minimizing the residual velocity dispersion. This was performed by applying the fitting method developed by Epinat et al. (2008; E08). We refer the reader to E08 for more details about the fitting procedure. The axisymmetric model for the velocity field is also shown in this panel by the smooth colored background in regions without observable H_{α} .

The observed V_{los} field contains contributions from the three different velocity components: the distributions within the disk plane, radial V_R and rotational, V_{ϕ} , and the perpendicular velocity to the disk plane, V_Z . To remove the modeled unperturbed V_{ϕ} velocity field from the observed V_{los} distribution, we subtract the axisymmetric kinematic model from the data. The residual velocity map, V_{res} , is shown in the bottom panel of Figure 3. The map shows a strong, global, and coherent pattern extending all the way to the disk outskirts, with V_{res} values that can be as large as 50 km s^{-1} .

The structure of the residual map is consistent with what is expected for the V_Z field of a corrugated disk galaxy. As shown by several previous studies (see, e.g., D’Onghia et al. 2016; Gómez et al. 2016, 2017; Laporte et al. 2018b) vertical velocity flows both in the disk stellar and gas components, caused by a recent interaction with an external perturber, are common and can reach these large amplitudes. These studies have also shown that vertical patterns in the cold star-forming gas and stellar components of a disk can remain coincident for more than 1 Gyr (Gómez et al. 2017). Given the large amplitudes of the perturbations observed in the VV304a V_{res} field ($\sim 50 \text{ km s}^{-1}$), a significant contribution from off-plane velocity flows, V_Z , induced by the recent interaction with VV304b,

¹⁰ <https://cgs.obs.carnegiescience.edu/CGS/Home.html>

¹¹ The code is available at <http://www.astro.umontreal.ca/fantommm/reduction/>.

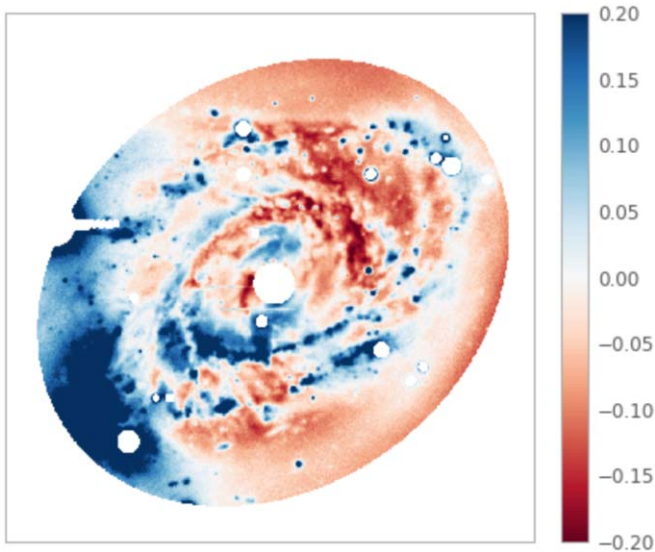


Figure 4. Estimated overdensity map of VV304a. The color bar indicates the value of $\Delta\rho = (\text{image} - \text{model})/\text{model}$. The light distribution model was obtained by fitting elliptical isophotes to the galaxy’s Gemini/GMOS r' -band image. The spiral structure of VV304a shows a density contrast with respect to the background disk of the order $\Delta\rho \lesssim 30\%$.

can thus be expected. The upper half of the V_{res} map shown in the middle panel of Figure 3 shows a particularly interesting feature, which covers approximately 180° of the galactic disk, extends to the outskirts of the disk, and has an amplitude of $\sim 40 \text{ km s}^{-1}$. Note how the disk’s V_{res} sharply transitions from large positive to negative values. Such behavior could indicate a significant displacement of the disk’s $\langle Z \rangle$ with respect to its overall midplane. A similar displacement has been observed in the outer Milky Way disk. Known as the Monoceros ring, this large and complex stellar structure exhibits a north–south asymmetry in $\langle Z \rangle$, with the southern and northern parts dominating the regions closer and farther from the Sun, respectively (e.g., Slater et al. 2014).

However, as previously discussed, due to the nonnegligible inclination of the VV304a disk and to the presence of spiral structure and a possible weak bar, the resulting V_{res} could contain significant contributions from in-plane velocity flows. Monari et al. (2016) studied the effects of bar–spiral coupling on stellar kinematics considering bars and spiral structure, similar to those observed in the Milky Way. They find that the in-plane velocity perturbations associated with these $m = 2$ patterns are $< 20 \text{ km s}^{-1}$ (see also Canzian 1993).

It is worth recalling that VV304a does not possess any strong $m = 2$ bar perturbation (see Section 2.1). However, it does show a flocculent-like spiral structure. To quantify the strength of this spiral structure, we generate a 2D model of the galaxy’s light distribution. We fit elliptical isophotes to the Gemini/GMOS r' -band image of the galaxy using the IRAF task ELLIPSE with a fixed ellipticity of 0.2. The 2D model is obtained using the isophotal results. Once the model is obtained, we generate a residual overdensity map by assuming a constant mass-to-light ratio across the disk. This is done by computing

$$\Delta\rho = \frac{\text{image} - \text{model}}{\text{model}}.$$

Note that, in this photometric band, departures from a constant mass-to-light ratio across the disk are expected to be small (see the Appendix for more details.)

The results of this procedure are shown in Figure 4, where the color coding indicates the value of $\Delta\rho$. The overdense region in the bottom left area of this figure is likely the result of the recent tidal interaction with VV304b, and can also be appreciated in the top panel of Figure 1. On the other hand, the underdense region in the top right area is the result of significant dust extinction (see also the top panel of Figure 1). In general, we find that the spiral structure of VV304a shows a density contrast with respect to the background disk of the order $\Delta\rho \lesssim 30\%$, similar to that observed in the Milky Way (see Monari et al. 2016 and references therein). In the following section we will use this information to further characterize the contribution from in-plane velocity flows that could arise from bars or a bisymmetric spiral structure to the V_{res} field of a low-inclination disk.

3. Analytical Models of Perturbed Velocity Fields

It is well known that radial and tangential flows can arise from the dynamical influence of a bar or spiral structure on a disk (Siebert et al. 2012; Grand et al. 2016b; Monari et al. 2016), and that the amplitudes of such flows vary with the strength of these $m = 2$ modes. To characterize the contribution from in-plane velocity flows driven by the VV304a nonaxisymmetric structure, we have run and analyzed a suite of test-particle simulations using a Milky Way–like galactic potential. The model parameters were chosen to reasonably reproduce the properties of VV304a listed in Section 2.1.

The analytic galactic model considers a Hernquist profile for the bulge component,

$$\Phi_{\text{bulge}} = -\frac{GM_{\text{bulge}}}{\sqrt{x^2 + y^2 + z^2} + \epsilon_{\text{bulge}}}, \quad (1)$$

with $M_{\text{bulge}} = 0.47 \times 10^{10} M_\odot$, $\epsilon_{\text{bulge}} = 0.83 \text{ kpc}$. To approximate a double exponential disk profile, we follow the procedure described by Smith et al. (2015). The idea behind this method is to approximate an exponential profile by the superposition of three different Miyamoto and Nagai (MN) profiles (Miyamoto & Nagai 1975). Smith et al. (2015) provides a user-friendly online form that computes the best-fitting parameters for an exponential disk¹²,

$$\rho(R, z) = \rho_0 \exp(-R/\epsilon_{\text{disc}}^s) \exp(-|z|/\epsilon_{\text{disc}}^h), \quad (2)$$

with $\rho(R, z)$ the axisymmetric density, $R = \sqrt{r^2 - z^2}$ the projected galactocentric distance, and ρ_0 the central density. Our resulting disk model has a total mass $M_{\text{disc}} = 5.9 \times 10^{10} M_\odot$, scale length $\epsilon_{\text{disc}}^s = 3.1 \text{ kpc}$ and scale height $\epsilon_{\text{disc}}^h = 0.3 \text{ kpc}$. For the dark matter halo we consider a Navarro–Frenk–White profile

$$\Phi_{\text{NFW}} = -\frac{A}{r} \ln \left[1 + \frac{r}{r_s} \right], \quad (3)$$

¹² <http://astronomy.swin.edu.au/~cflynn/expmaker.php>

where

$$A = \frac{GM_{200}}{\ln(1 + c_{\text{NFW}}) - \frac{c_{\text{NFW}}}{1 + c_{\text{NFW}}}},$$

with $M_{200} = 1.45 \times 10^{12} M_{\odot}$, $r_{200} = 234.5$ kpc yr, and $r_s = 14.6$ kpc. Note that these parameter choices yield a total dynamical mass within 18 kpc of $\approx 2.55 \times 10^{11} M_{\odot}$ and peak circular velocity of 250 km s^{-1} , in good agreement with VV304a.

Following Monari et al. (2016, hereafter M16) we include a 3D bar potential, described by

$$\Phi_{\text{bar}}(R, \phi, z, t) = \alpha \frac{v_0^2}{3} \left(\frac{R_0}{R_b} \right)^3 U(r) \frac{R^2}{r^2} \cos(\gamma_b), \quad (4)$$

where R_b is the length of the bar, v_0 is the circular velocity at R_0 , $\gamma_b(\phi, t) \equiv 2(\phi - \phi_b - \Omega_b t)$, and

$$U(r) \equiv \begin{cases} -(r/R_b)^{-3} & \text{for } r \geq R_b, \\ (r/R_b)^3 - 2 & \text{for } r < R_b. \end{cases} \quad (5)$$

The amplitude α is the ratio between the bar and the axisymmetric contribution to the radial force along the bar's long axis at $(R, z) = (R_0, 0)$. Even though, as previously shown, VV304a does not present a well-defined bar perturbation, we included in our suite a model with a bar with similar characteristic to that of the Milky Way. This is $\alpha = 0.01$, $\Omega_b = -52.2 \text{ km s}^{-1} \text{ kpc}^{-1}$, and $R_b = 3.5$ kpc. This last model also includes a spiral perturbation with a 200% density contrast.

Finally, as in M16, we introduce a 3D spiral perturbation consisting of a two-armed model as proposed by Cox & Gómez (2002),

$$\Phi_{\text{spiral}}(R, \phi, z, t) = -\frac{A}{R_s K D} \cdot e^{-\frac{(R-R_s)}{R_{sd}}} \cos(\gamma_s) \left[\text{sech} \left(\frac{Kz}{\beta} \right) \right]^\beta, \quad (6)$$

where

$$\begin{aligned} K(R) &= \frac{2}{R \sin(p)}, \\ \beta(R) &= K(R) h_s [1 + 0.4K(R) h_s], \\ D(R) &= \frac{1 + K(R) h_s + 0.3[K(R) h_s]^2}{1 + 0.3K(R) h_s}, \\ \gamma_s(R, \phi, t) &= 2 \left[\phi - \phi_s - \Omega_s t - \frac{\ln(R/R_s)}{\tan p} \right]. \end{aligned} \quad (7)$$

Here, p is the pitch angle, A the amplitude of the spiral potential, h_s controls the scale height of the spiral, and R_s is the reference radius for the angle of the spirals. We choose $R_s = 1$ kpc, $R_{sd} = 3.1$ kpc, $\Omega_s = -18.9 \text{ km s}^{-1} \text{ kpc}^{-1}$, and $p = 9.9^\circ$. For our study, the most relevant parameter is A , which sets the strength of the perturbation. When modeling the Milky Way M16 considered two values of A . The first, $A = 341.8 \text{ km}^2 \text{ s}^{-2}$ and referred to as ‘‘reference spirals’’, corresponds to a 30% density contrast of the spiral arms with respect to the background disk surface density at $R = R_0 = 8$ kpc. A second model, referenced to as ‘‘strong

spirals’’, considers $A = 683.7 \text{ km}^2 \text{ s}^{-2}$, i.e., a 60% density contrast. These values of A result in a maximum radial force exerted by the spiral arms of 0.5% and 1% of the force due to the axisymmetric background at R_0 , and introduced velocity perturbation in V_R and $V_\phi < 15 \text{ km s}^{-1}$. As previously discussed in Section 2.3, the strength of the VV304a spiral structure lies in between the M16 reference and strong models. Nonetheless, in this work we are interested in exploring how strong a spiral perturbation should be in order to induce perturbation in the V_{los} field as large as those observed in VV304a (i.e., $\sim 50 \text{ km s}^{-1}$). For this purpose, we also explore significantly larger values of A , namely a 100%, 200%, 600%, and 1000% density contrast, $\Delta\rho$, with respect to the background disk surface density at R_0 . The later model translates into a maximum radial force exerted by the spiral arms of $\sim 17\%$ of the force due to the axisymmetric background at R_0 .

For each model a set of $\sim 5 \times 10^6$ test particles, sampling the phase-space distribution of the unperturbed stellar disk, were initialized in equilibrium using the publicly available code MAGI¹³ (Miki & Umemura 2018). The initial conditions were integrated using another publicly available code, LP-VIcode¹⁴ (Carpintero et al. 2014) to make them evolve for 9.6 Gyr to allow the system to relax. This integration time was chosen so that any spurious substructures on the disk density field, arising due to the unrelaxed set of initial conditions, are well mixed within the inner 20 kpc. After that period of time, the nonaxisymmetric perturbations to the potential were slowly introduced by linearly increasing in time their amplitude to the desired value. Following Monari et al. (2016), this was done within a period of 3 Gyr, which represents ≈ 15 full rotations of nonaxisymmetric perturbations. Finally, each model was allowed to evolve under the influence of the perturbed potential for an additional period of 3 Gyr.

In Figure 5 we show the resulting V_{los} map for each model, after rotating them into an inclination of 35° and a position angle of 105° to emulate the orientation of VV304a. To compute the V_{los} we subtracted from each particle's V_ϕ the circular velocity at the corresponding galactocentric radii. To highlight the effect of the nonaxisymmetric perturbation, the color bars in the top panels have been scaled based the maximum V_{los} value obtained on each map. The leftmost panel shows the results obtained for the $\Delta\rho = 100\%$ model, similar to the strong spiral model of M16 ($\Delta\rho = 60\%$). As expected, our results are in good agreement with those of M16 (see their Figure 5). After inclining the disk to $i = 35^\circ$, the resulting perturbation in the V_{los} field is of the order of only 1 km s^{-1} . As we increase the strength of the spiral perturbation, the magnitude of the in-plane flows significantly increases, reaching values of 10 km s^{-1} for our most extreme model, i.e., $\Delta\rho = 1000\%$. The second and third panels show a comparison between models without and with bars, respectively. Both models include a spiral perturbation with $\Delta\rho = 200\%$. Note that the bar enhances the magnitude of the in-plane flows in the very inner disk regions, doubling its amplitude with respect to the barless model. Yet, even with the bar included, the V_{los} perturbations reach values $< 6 \text{ km s}^{-1}$. In the bottom panels of Figure 5, for comparison, we show the same models but now the color bars have been set as in the bottom panel of Figure 3.

¹³ <https://bitbucket.org/ymiki/magi>

¹⁴ <http://lp-vicode.fcaglp.unlp.edu.ar/>

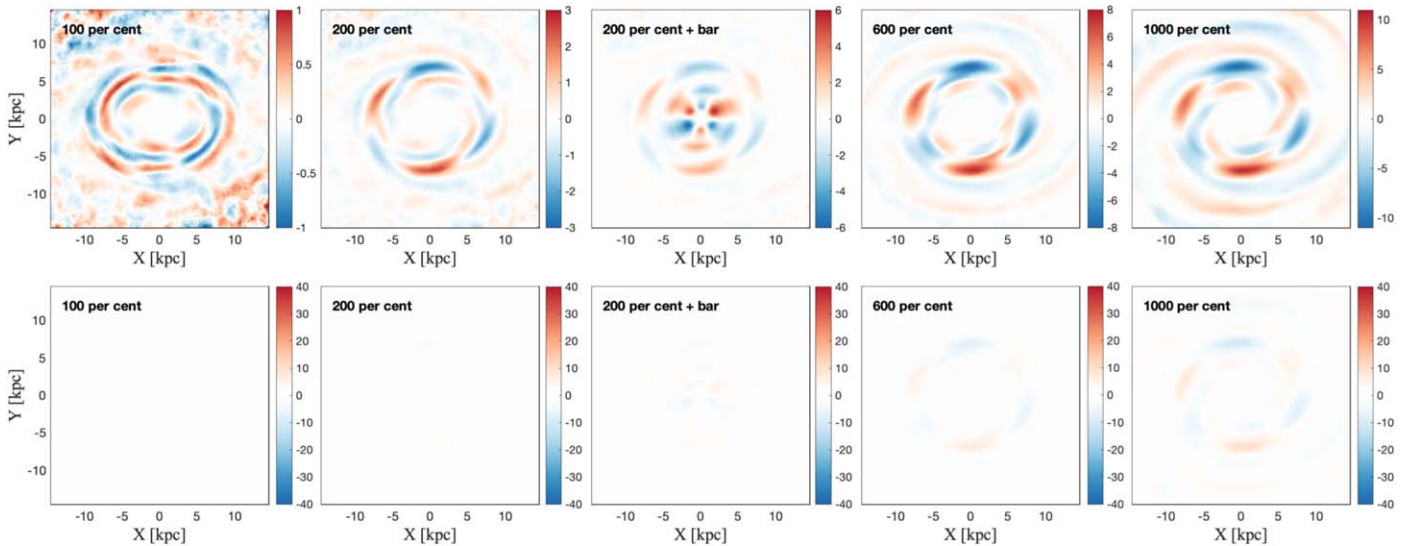


Figure 5. V_{los} maps from our suite of test-particle simulations, obtained after rotating the models to emulate the orientation of VV304a, ($i = 35^\circ$, $\text{PA} = 105^\circ$). The top left corner of each panel indicates the value of the density contrast at R_0 of the spiral structure, $\Delta\rho$, with respect to the background disk surface density. The third panel also includes the contribution from a galactic bar with similar parameters to those of the Milky Way’s bar. The color bar in the top panels is scaled to the corresponding maximum V_{los} value. For comparison, the color bars in the bottom panels have been scaled as in the bottom panel of Figure 3. Note that even our strongest spiral model, $\Delta\rho = 1000$, cannot generate in-plane velocity perturbations as large as those seen in VV304a.

This figure clearly shows that, for a galaxy with $i = 35^\circ$, neither a bar as strong as the one of the Milky Way nor a spiral structure with a $\Delta\rho$ as large as 1000% can secularly introduce perturbations in the V_{los} field with amplitudes as large as those observed in VV304a. We recall that VV304a does not show a bar and that the $\Delta\rho$ of its spiral structure is $<100\%$ of the background density of its disk.

In this section we have analyzed the secular response of a disk to a bar and spiral perturbation using test-particle simulations of an isolated galaxy. In what follows we use highly resolved fully cosmological self-consistent hydrodynamical simulations to characterize the impact that in-plane velocity flows, associated with both strong and mild $m = 2$ modes, can have on the V_{res} field of a galactic disk that has recently interacted with an external perturber.

4. Self-consistent Models of Perturbed Velocity Fields

In the previous section we used a suite of test-particle simulations to show that the VV304a spiral structure cannot secularly drive in-plane flows that are sufficiently large enough to account for the velocity perturbation observed in its V_{res} field. In this section we further study the impact that in-plane flows may have on the V_{res} field of this low-inclination interacting galaxy by analyzing a fully self-consistent cosmological simulation of VV304a-like models. We have focused on models that have recently interacted with an external companions and that present (i) weak and (ii) very strong $m = 2$ modes.

The main advantage of using fully cosmological simulations, as opposed to tailored simulations of interacting galaxies set in isolation, is that the former self-consistently include mechanisms that can significantly perturb an otherwise initially relaxed disk, such as previous close encounters with satellites, distant flybys of massive objects, and accretion of misaligned cold gas from halo infall or from mergers. Thus a realistic representation of possible sources of confusion is included in our study.

4.1. The Auriga Models

The Auriga project (Marinacci et al. 2014; Grand et al. 2017, 2019) consists of ~ 40 high-resolution cosmological zoom-in simulations of the formation of late-type galaxies within Milky Way–sized halos, performed with the N -body, magnetohydrodynamics code AREPO (Springel 2010). The code includes modeling of a wide range of critical physical processes that govern galaxy formation (Marinacci et al. 2014) such as gas cooling/heating, star formation, mass return, and metal enrichment from stellar evolution, the growth of a supermassive black hole, and feedback from stellar sources and from black hole accretion. The halos were selected from a lower-resolution dark-matter-only simulation from the Eagle Project, a periodic cube of side length 100 comoving Mpc (Schaye et al. 2015). Each halo was chosen to have, at $z = 0$, a virial mass in the range of $0.5\text{--}2 \times 10^{12} M_\odot$ and to be more distant than nine times the virial radius from any other halo of mass more than 3% of its own mass. The dark matter particle and gas cell mass for the simulation considered here are $\sim 3 \times 10^5 M_\odot$ and $\sim 5 \times 10^4 M_\odot$, respectively. The gravitational softening length of the stars and dark matter grows with a scale factor up to a maximum of 369 pc, after which it is kept constant in physical units. The softening length of gas cells scales with the mean radius of the cell, but is never allowed to drop below the stellar softening length. A study across three resolution levels shows that many galaxy properties, such as surface density profiles, orbital circularity distributions, star formation histories, and disk vertical structures are already well converged at the resolution level considered in this work.

Previous studies based on the same simulations have shown that vertical patterns in the cold star-forming gas and stellar components of a disk can remain coincident for more than 1 Gyr (Gómez et al. 2017). Thus, we focus on the stellar components which have much better spatial resolution compared to the cold gas disks. Nevertheless, it is worth noticing that the vertical pattern in the two models considered here can also be recovered from the cold star-forming gas distribution.



Figure 6. Present day stellar distribution of the Aq-C4 disk. The images were constructed by mapping the K -, B -, and U -band luminosities to the red, green, and blue channels of a full color composite image. Younger (older) star particles are therefore represented by bluer (redder) colors. The left and right panels show the edge-on and face-on views, respectively. Note the simulated disk shows a weak bar and multiarm spiral structure, similar to what is observed in the VV304a disk. Figure from Marinacci et al. (2014).

4.1.1. Weak $m = 2$ Model

We first analyze the Aq-C4 model, first introduced in Marinacci et al. (2014). Aq-C4 has the property of being one of the most similar models to the Milky Way within the sample. It has a flat rotation curve that peaks at 250 km s^{-1} at $\sim 4 \text{ kpc}$. Its disk scale length and bulge effective radius are approximately 3.1 and 0.8 kpc, respectively. At present it has $M_{\text{tot}} \sim 1.46 \times 10^{12} M_{\odot}$, a baryonic disk + bulge mass $M_{*} \sim 5.3 \times 10^{10} M_{\odot}$, and a disk optical radius of $\sim 20 \text{ kpc}$. Here we define the optical radius as the radius where $\mu_{\text{B}} = 25 \text{ mag arcsec}^{-2}$ (see Pranav & Jog 2010). Note that these properties make Aq-C4 a very reasonable model of VV304a (see Section 2.1). Aq-C4 shows a quiet formation history since $z \approx 1$, without any close interaction with satellites more massive than $M_{\text{sat}}/M_{\text{host}} = 1/40$. The most significant perturber is a low-velocity flyby with a pericenter passage of 80 kpc at a lookback time of $t_{\text{look}} \approx 2.7 \text{ Gyr}$. The satellite has a total mass of $\sim 4 \times 10^{10} M_{\odot}$ ($M_{\text{sat}}/M_{\text{host}} \approx 1/50$). As shown in Gómez et al. (2016) the satellite is not massive enough to directly perturb the galactic disk but the density field of the host dark matter halo responds to this interaction resulting in a strong amplification of the perturbative effects. The resulting dark matter wake is efficiently transmitted to the inner parts of the host perturbing the embedded disk. This perturbation causes the onset and development of a vertical pattern, similar to the Monoceros ring. Figure 6 shows the present day stellar distribution. The disk has a weak bar and weak multiarm spiral structure, similar to that observed in the VV304a galactic disk. The green line in Figure 8 shows the time evolution of the amplitude of the $m = 2$ mode in Aq-C4’s disk, computed within the inner 20 kpc following the approach of Grand et al. (2016a).

4.1.2. Strong $m = 2$ Model

Among the Auriga models, Au25 is the one that most closely resembles the VV304 system in terms of its global properties. Furthermore, as discussed below, it has the strongest $m = 2$ close to $z = 0$. The host galaxy has, at the present day, a total mass of $M_{\text{tot}} \sim 1.25 \times 10^{12} M_{\odot}$, a baryonic disk + bulge mass

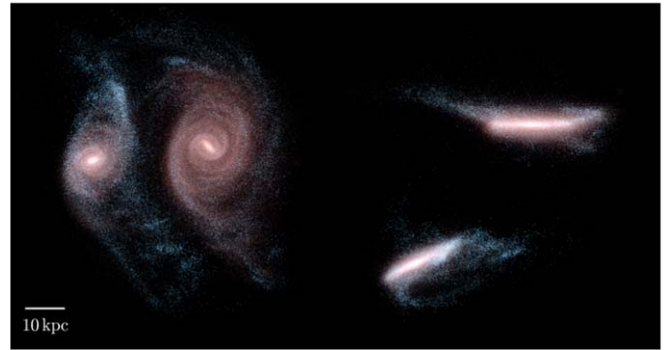


Figure 7. The moment of closest approach between the simulated Auriga galaxy, Au25, and its massive companion. The images were created as in Figure 6. The face-on (left) and edge-on (right) views are oriented with respect to the Au25 disk. The disk shows a strong bar and a grand design spiral structure.

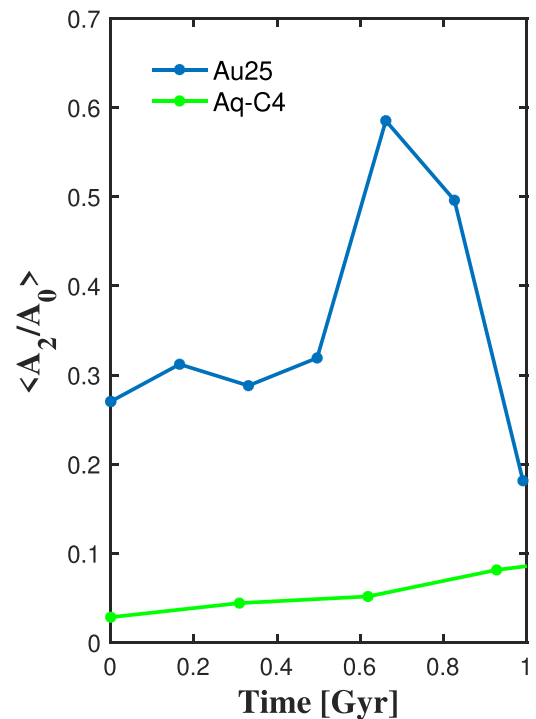


Figure 8. The time evolution of the amplitudes of the $m = 2$ Fourier mode of the simulated stellar disks analyzed in this work. The green and blue lines show results for the Aq-C4 and Au25 disks, respectively.

of $M_{*} \sim 3.4 \times 10^{10} M_{\odot}$, a peak circular velocity of $\sim 180 \text{ km s}^{-1}$, and a disk optical radius that azimuthally varies between 21 and 30 kpc. Even though Au25 is slightly less massive than VV304a, it had a close encounter with a massive satellite 0.9 Gyr ago whose total mass at infall was $M_{\text{sat}} \sim 3 \times 10^{11} M_{\odot}$ and whose orbit reached the host’s inner 40 kpc. This configuration is reminiscent of the recent interaction in VV304a and b. Figure 7 highlights the moment of closest approach. During the interaction, the host galaxy is strongly tidally perturbed and develops a significant misalignment of its outer dark matter halo regions. The interaction also induces the formation of two tidal arms and triggers strong vertical patterns whose signatures can still be detected clearly at the present day (Gómez et al. 2017). Note the 1:4 host to satellite mass ratio, which can be classified as a massive interaction. In Figure 8 we show the time evolution of its

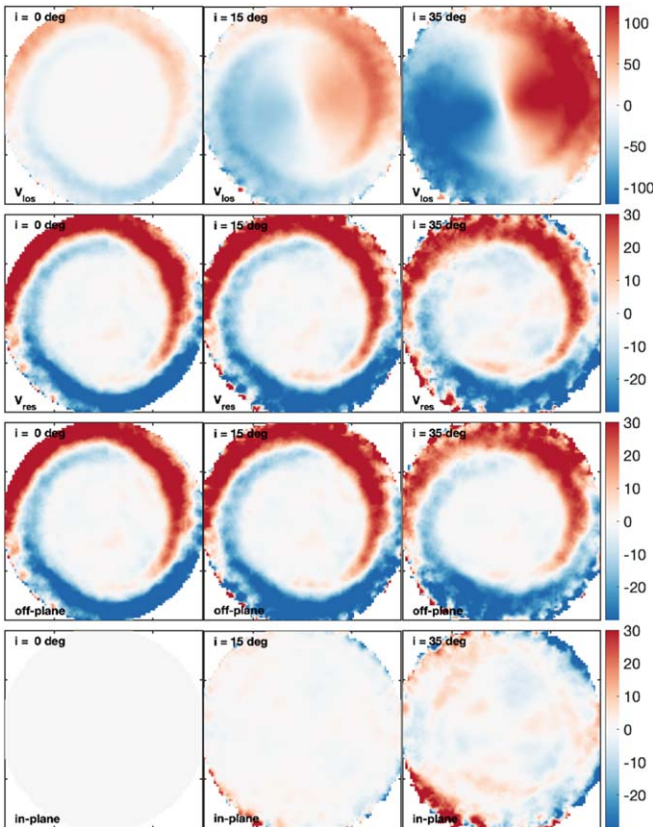


Figure 9. First row: Aq-C4 line-of-sight velocity field, V_{los} , obtained for three different inclination angles. From left to right we show the maps after tilting the disk by $i = 0^\circ$, 15° , and 35° , respectively. The second row shows residual velocity maps, V_{res} , obtained after subtracting from every stellar particle the mean rotation velocity at the corresponding radial position. The third and fourth rows show the contributions from vertical and in-plane motions to the V_{res} fields, respectively. Note that even at $i = 35^\circ$ V_{res} is dominated by vertical motions, V_z .

$m = 2$ mode, measured as in Section 4.1.1. The interaction with its massive companion triggers the development of a strong $m = 2$ signal associated with both a galactic bar and grand design spiral structure (see Figure 12). Grand et al. (2016a) studied the time evolution of the $m = 2$ modes on a large sample of the Auriga models. Figure 4 of that work shows that Au25 has the strongest $m = 2$ mode during the last 3 Gyr of evolution.

4.2. Simulated Residual V_{los} Fields

To investigate whether our simulated disks develop similar velocity patterns to those observed in VV304a, we first rotate the main host disks to an inclination of $i = 35^\circ$ and $PA = 100^\circ$, similar to the values estimated for VV304a. We then compute maps of mean V_{los} across the disk plane for all snapshots after the interactions. The top rightmost panels of Figures 9 and 10 show an example of the V_{los} map obtained from the Aq-C4 and Au25 disks, respectively. The snapshot corresponds to $z = 0$ for Aq-C4, 2.4 Gyr after the flyby closest approach, and ~ 0.75 Gyr after the strong interaction suffered by Au25, just one snapshot before $z = 0$. Although some interesting departures from perfectly rotating disks can be observed, in both cases the resulting maps are clearly dominated by the V_ϕ velocity component.

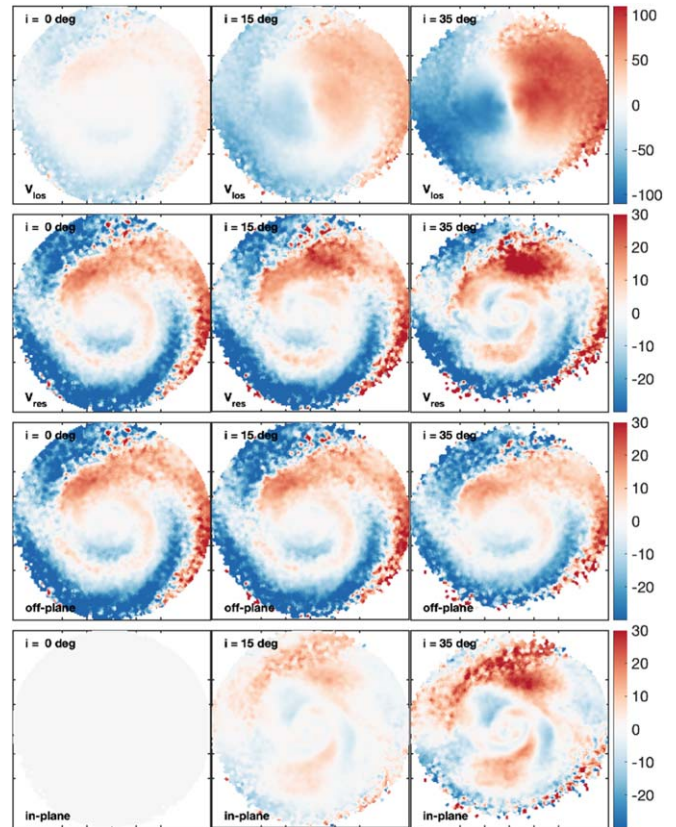


Figure 10. As Figure 9, but for Au25.

To obtain the V_{res} velocity field for the simulated stellar disks, we subtract from every stellar particle the mean rotation velocity at the corresponding radial position. The resulting maps are shown on the right panels of the second rows of Figures 9 and 10. As in the VV304a case, the V_{res} maps show strong and coherent velocity patterns that can reach amplitudes as large as 50 km s^{-1} . Note that both maps show similarly strong flows, despite the differing strength of their in-plane disk $m = 2$ modes. The morphology of the coherent flows shows very similar features to those in the observational data, with sharp transitions between positive and negative V_{res} velocities. Such transitions are associated with extrema in the displacement of the midplane of the disks if the V_{res} fields are indeed dominated by off-plane motions, V_z . To explore this, we show on the second row of Figures 9 and 10 the V_{res} maps obtained after inclining the disk by only 15° (second panel) and 0° (first panel). Note that in a perfectly face-on configuration, i.e., $i = 0^\circ$, the resulting V_{los} and V_{res} maps are equivalent to the disk's mean vertical velocity distribution, V_z . Thus, coherent and extended departures from 0 km s^{-1} on these maps are a direct indication of a corrugation in the simulated host disks.

It is clear in both cases that the patterns seen in the V_{res} field are preserved as we tilt the disks toward lower inclinations. In the case of Aq-C4, these are not only preserved but the amplitude of the patterns increases for lower inclination angles. This indicates a negligible contribution from in-plane flows to the V_{res} field, even at $i = 35^\circ$. This is not surprising since, as in the case of VV304a, the simulated disk shows a very mild $m = 2$ pattern. A similar result is found for Au25 (see Figure 10). The global morphology of the V_{res} field is preserved as we decrease the inclination. The $i = 0^\circ$ map reveals very strong vertical flows, with amplitudes larger than

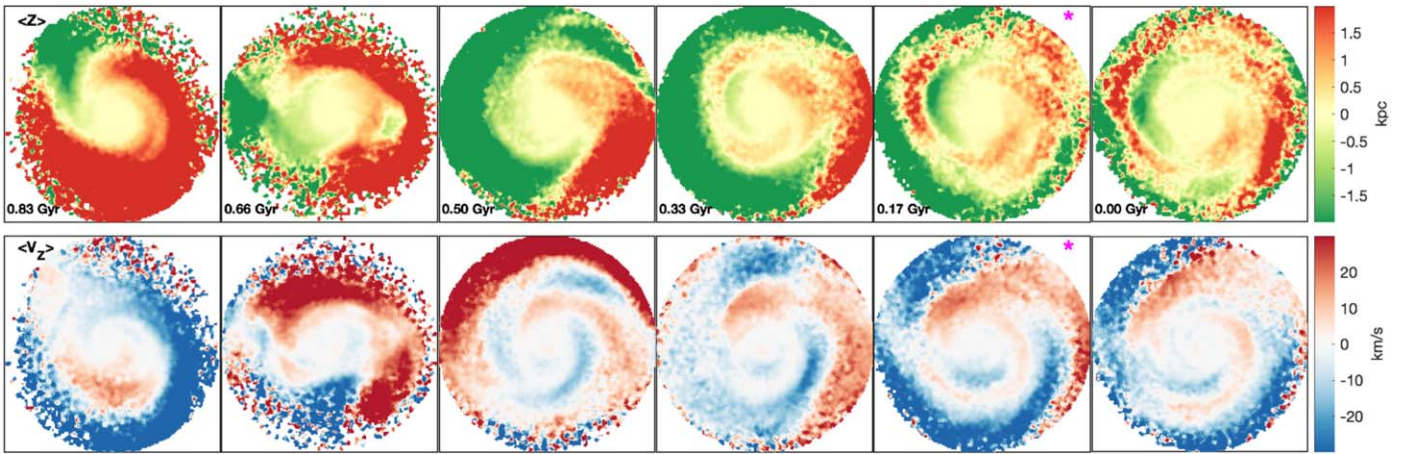


Figure 11. Time evolution of the vertical structure of the disk in Au25 over a period of ~ 1 Gyr. The top panels show maps of the mass-weighted $\langle Z \rangle$. The bottom panels show maps of the mass-weighted $\langle V_Z \rangle$. The onset-time of the vertical perturbation is $1 \gtrsim t_{\text{onset}} \gtrsim 0.8$ Gyr, coinciding with the pericenter passage of the most massive satellite. The perturbation starts as a $m = 1$ mode that winds up in time. The snapshot used for comparison with the VV304a data is highlighted with the magenta stars (second from right). In this projection the galactic disk rotates counterclockwise.

40 km s^{-1} , that are the result of disk corrugation. Note the trailing nature of this corrugation pattern. Contrary to the Aq-C4 case, where leading patterns develop over time due to the inner disk torque (Shen & Sellwood 2006; Gómez et al. 2016), the vertical structure of the Au25 disk traces the trailing structure of the tidal arms created during the recent interaction.

It is clear that vertical flows dominate the $i = 35^\circ$ V_{res} field in the Au25 disk. However the amplitudes of some of these features decrease for lower inclination, indicating a nonnegligible contribution from in-plane flows. To further characterize the contribution from the different velocity components, we show velocity maps in Figures 9 and 10 in which only vertical (third row) and in-plane (fourth row) motions are included. For Aq-C4 (weak $m = 2$ mode) it is clear that the contribution from in-plane flows is negligible, even at $i = 35^\circ$. In the Au25 case (strong $m = 2$), even though significant in-plane flows can be found at certain locations, the off-plane flows dominate the total residual velocity patterns over most of the disk, even at $i = 35^\circ$. This shows that the velocity perturbations seen in the inclined simulated disk are indeed primarily associated with a corrugation pattern.

Clearly, features in the V_{res} map of a low-inclination disk that has recently interacted with a companion can be dominated by flows in the direction perpendicular to the disk plane. We recall that this is true even for Au25 which shows the strongest in-plane $m = 2$ pattern in the Auriga sample close to $z = 0$. The disk of VV304a shows neither a strong bar nor a grand design spiral and thus more closely resembles the structure seen in Aq-C4. This suggests that the global and coherent velocity patterns seen in VV304a could indeed be associated with vertical flows.

In Figure 11 we show the time evolution of the mean height, $\langle Z \rangle$ (top), and mean vertical velocity, $\langle V_Z \rangle$ (bottom), of the stellar disk in Au25. A similar figure for Aq-C4 can be found in Figure 3 of Gómez et al. (2016). This period of time covers the satellite’s closest approach and the snapshot used for data to model comparison, indicated with a magenta star. The link between the onset of the disk vertical perturbation and closest approach of the most massive companion, at $t \sim 1$ Gyr, is evident. Notice how the vertical perturbation starts as an $m = 1$ pattern that winds up as time goes by. The counterparts of the extended and coherent structures seen in the $\langle V_Z \rangle$ and inclined V_{res} fields at $t = 0.17$ and 0 Gyr are clearly associated with a

vertical displacement of the disk with respect to the overall midplane. These structures resemble one of the largest vertical asymmetries of our own Galactic disk: the Monoceros ring. A similar feature is seen in the V_{res} field of VV304a (bottom panel of Figure 3), which strongly suggests the presence of a Monoceros ring-like feature in this external late-type galaxy.

The origin of the Monoceros ring has been a puzzle for many years and it has been debated whether its constituent stars are the debris of a disrupted satellite galaxy or whether the structure is the projection of a corrugation pattern in our own disk (see Guglielmo et al. 2018; Laporte et al. 2018b and references therein).

5. Conclusions

In this work we have analyzed the 2D V_{los} field of the late-type galaxy VV304a, obtained through H_α Fabry–Perot observations. In many aspects, VV304a can be considered a Milky Way analog which is currently interacting with a massive companion, VV304b. After subtracting an axisymmetric kinematic model from the observed V_{los} field, we find that the residuals show strong, global, and coherent motions which are consistent with a corrugation pattern. The contribution from in-plane flows to the V_{res} field cannot be subtracted with the available data. However, nonaxisymmetric features such as spiral arms and/or a bar are much too weak in VV304a to generate line-of-sight perturbations as large as those measured. We have demonstrated this by analyzing multiband images of VV304a, and comparing them to a suite of test-particle simulations of nonaxisymmetric galaxies with bars and an $m = 2$ spiral structure but no extraplanar perturbations. Even spiral arms an order of magnitude stronger than those observed in VV304a do not induce velocity flows strong enough to explain the perturbations seen in its V_{res} field. Based on these results, we analyzed fully cosmological models with strong and weak $m = 2$ patterns to explore whether the V_{res} field of a galaxy that recently interacted with an external perturber could still be dominated by signatures of a corrugation pattern, even for a disk as inclined as VV304a. Our results show that this can indeed be the case.

The VV304a V_{res} map hints at a structure that resembles the Monoceros ring, an extended low-latitude stellar overdensity in

our own Galaxy which may therefore be associated with a global disk corrugation pattern. Several recent studies have linked this structure to interactions with the Sgr dwarf galaxy (Purcell et al. 2011; Gómez et al. 2013; Laporte et al. 2018b), even though its origin is still being debated. Note that although Sgr was likely less massive at infall than VV304b, several different arguments suggest a total infall mass of the order of $\gtrsim 10^{11} M_{\odot}$ (e.g., Purcell et al. 2011); this could thus be a 1:10 interaction. As shown in Gómez et al. (2017), strong global corrugation patterns can be induced during such interactions.

Our results demonstrate that it is possible to address important questions regarding the nature and origin of vertical perturbations by measuring the velocity distribution of nearby nearly face-on galaxies. What is the prevalence of vertical corrugation patterns in the local universe? What are the main physical mechanisms behind the formation of such patterns? And what can they tell us about the recent interaction history of their host galaxies? The tidal origin of VV304a's perturbation is very clear: a close interaction with VV304b. However, the presence of a corrugation pattern could also be used to constrain the asymmetries of the host dark matter halo and to study unseen structure in the outskirts of galaxies (Vesperini & Weinberg 2000; Gómez et al. 2016). Our study opens a new window into investigating whether the corrugation pattern observed in the Milky Way disk is a rare or common feature of late-type galaxies.

F.A.G. and C.M. acknowledge financial support from FONDECYT Regular 1181264. F.A.G., A.M., and C.M. acknowledge funding from the Max Planck Society through a Partner Group grant. A.M. acknowledges financial support from FONDECYT Regular 1181797. F.M. acknowledges support through the Program "Rita Levi Montalcini" of the Italian MIUR.

Appendix

M/L Ratios across a Simulated Disk

In order to test whether the assumption of a mass-to-light (*M/L*) ratio across the disk is reasonable, we computed the *M/L* ratio map for the galactic disk of the Au25 model. The map is shown in Figure 12. As in VV304a observations, we have focused on the *r'*-band. The reason behind this choice is that this band is a better tracer of the overall mass distribution than bluer photometric bands. As we can see from this figure, our model indicates an average *M/L* of the order 1 throughout the disk, with values that can vary between 0.2 to 2.75. This indicates that assuming a constant *M/L* in the analysis shown in Section 2.3 is a reasonable approximation in this case. Note that our goal in that section is to estimate the strength of the spiral structure in terms of its overdensity pattern. Our study suggests that the spiral structure of VV304a is $\sim 30\%$ denser than the background density of the overall disk. However, in our analytic model, we have gone as far as considering spiral structures that are 1000% denser than the background density. Thus, we expect small departures from a constant *M/L* to be covered by our most extreme models.

ORCID iDs

Facundo A. Gómez <https://orcid.org/0000-0002-1947-333X>
Antonela Monachesi <https://orcid.org/0000-0003-2325-9616>

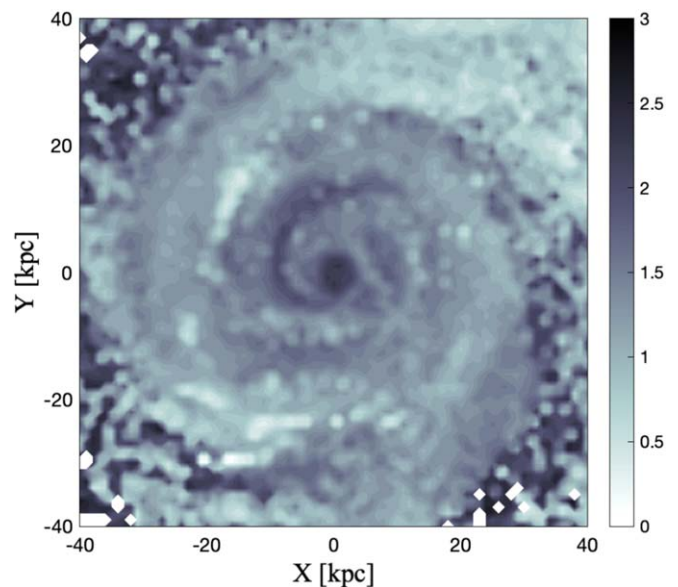


Figure 12. The color coding indicates the values of the simulated mass-to-light ratio in the *r'*-band, *M/L*, obtained across the disk of the cosmological simulation Au25. Values vary between *M/L* ~ 0.2 and 2.75.

Robert J. J. Grand <https://orcid.org/0000-0001-9667-1340>
Federico Marinacci <https://orcid.org/0000-0003-3816-7028>
Rüdiger Pakmor <https://orcid.org/0000-0003-3308-2420>
Volker Springel <https://orcid.org/0000-0001-5976-4599>
Carlos S. Frenk <https://orcid.org/0000-0002-2338-716X>

References

- Alfaro, E. J., Pérez, E., González Delgado, R. M., Martos, M. A., & Franco, J. 2001, *ApJ*, 550, 253
- Ann, H. B., & Park, J.-C. 2006, *NewA*, 11, 293
- Antoja, T., Helmi, A., Romero-Gómez, M., et al. 2018, *Natur*, 561, 360
- Bland-Hawthorn, J., Sharma, S., Tepper-García, T., et al. 2019, *MNRAS*, 486, 1167
- Boselli, A., Fossati, M., Ferrarese, L., et al. 2018, *A&A*, 614, A56
- Canzian, B. 1993, *ApJ*, 414, 487
- Carpintero, D. D., Maffione, N., & Darriba, L. 2014, *A&C*, 5, 19
- Cautun, M., Benítez-Llambay, A., Deason, A. J., et al. 2020, *MNRAS*, 494, 4291
- Cox, D. P., & Gomez, G. C. 2002, *ApJS*, 142, 261
- Daigle, O., Carignan, C., Hernandez, O., Chemin, L., & Amram, P. 2006, *MNRAS*, 368, 1016
- D'Onghia, E., Madau, P., Vera-Ciro, C., Quillen, A., & Hernquist, L. 2016, *ApJ*, 823, 4
- Epinat, B., Amram, P., Marcelin, M., et al. 2008, *MNRAS*, 388, 500
- Fridman, A. M., Koruzhii, O. V., Zasov, A. V., et al. 1998, *AstL*, 24, 764
- Gaia Collaboration, Katz, D., Antoja, T., et al. 2018, *A&A*, 616, A11
- Gómez, F. A., Minchev, I., O'Shea, B. W., et al. 2012, *MNRAS*, 423, 3727
- Gómez, F. A., Minchev, I., O'Shea, B. W., et al. 2013, *MNRAS*, 429, 159
- Gómez, F. A., White, S. D. M., Grand, R. J. J., et al. 2017, *MNRAS*, 465, 3446
- Gómez, F. A., White, S. D. M., Marinacci, F., et al. 2016, *MNRAS*, 456, 2779
- Gómez-López, J. A., Amram, P., Epinat, B., et al. 2019, *A&A*, 631, A71
- Grand, R. J. J., Gómez, F. A., Marinacci, F., et al. 2017, *MNRAS*, 467, 179
- Grand, R. J. J., Springel, V., Gómez, F. A., et al. 2016a, *MNRAS*, 459, 199
- Grand, R. J. J., Springel, V., Kawata, D., et al. 2016b, *MNRAS*, 460, L94
- Grand, R. J. J., van de Voort, F., Zjupa, J., et al. 2019, *A&A*, 490, 4786
- Guglielmo, M., Lane, R. R., Conn, B. C., et al. 2018, *MNRAS*, 474, 4584
- Ho, L. C., Li, Z.-Y., Barth, A. J., Seigar, M. S., & Peng, C. Y. 2011, *ApJS*, 197, 21
- Laporte, C. F. P., Gómez, F. A., Besla, G., Johnston, K. V., & Garavito-Camargo, N. 2018a, *MNRAS*, 473, 1218
- Laporte, C. F. P., Johnston, K. V., Gómez, F. A., Garavito-Camargo, N., & Besla, G. 2018b, *MNRAS*, 481, 286
- Laporte, C. F. P., Minchev, I., Johnston, K. V., & Gómez, F. A. 2019, *MNRAS*, 485, 3134

- Liu, C., Xu, Y., Wan, J.-C., et al. 2017, *RAA*, **17**, 096
- Marinacci, F., Pakmor, R., & Springel, V. 2014, *MNRAS*, **437**, 1750
- McMillan, P. J. 2017, *MNRAS*, **465**, 76
- Miki, Y., & Umemura, M. 2018, *MNRAS*, **475**, 2269
- Miyamoto, M., & Nagai, R. 1975, *PASJ*, **27**, 533
- Monari, G., Famaey, B., Siebert, A., et al. 2016, *MNRAS*, **461**, 3835
- Muñoz-Elgueta, N., Torres-Flores, S., Amram, P., et al. 2018, *MNRAS*, **480**, 3257
- Newberg, H. J., Yanny, B., Rockosi, C., et al. 2002, *ApJ*, **569**, 245
- Pogge, R. W., & Martini, P. 2002, *ApJ*, **569**, 624
- Pranav, P., & Jog, C. J. 2010, *MNRAS*, **406**, 576
- Price-Whelan, A. M., Johnston, K. V., Sheffield, A. A., Laporte, C. F. P., & Sesar, B. 2015, *MNRAS*, **452**, 676
- Purcell, C. W., Bullock, J. S., Tollerud, E. J., Rocha, M., & Chakrabarti, S. 2011, *Natur*, **477**, 301
- Reshetnikov, V., & Combes, F. 1998, *A&A*, **337**, 9
- Sánchez-Gil, M. C., Alfaro, E. J., & Pérez, E. 2015, *MNRAS*, **454**, 3376
- Schaye, J., Crain, R. A., Bower, R. G., et al. 2015, *MNRAS*, **446**, 521
- Sheffield, A. A., Price-Whelan, A. M., Tzanidakis, A., et al. 2018, *ApJ*, **854**, 47
- Shen, J., & Sellwood, J. A. 2006, *MNRAS*, **370**, 2
- Siebert, A., Famaey, B., Binney, J., et al. 2012, *MNRAS*, **425**, 2335
- Slater, C. T., Bell, E. F., Schlafly, E. F., et al. 2014, *ApJ*, **791**, 9
- Smith, R., Flynn, C., Candlish, G. N., Fellhauer, M., & Gibson, B. K. 2015, *MNRAS*, **448**, 2934
- Springel, V. 2010, *MNRAS*, **401**, 791
- Torres-Flores, S., Amram, P., Mendes de Oliveira, C., et al. 2014, *MNRAS*, **442**, 2188
- Vesperini, E., & Weinberg, M. D. 2000, *ApJ*, **534**, 598
- Widrow, L. M., Gardner, S., Yanny, B., Dodelson, S., & Chen, H.-Y. 2012, *ApJL*, **750**, L41
- Xu, Y., Newberg, H. J., Carlin, J. L., et al. 2015, *ApJ*, **801**, 105
- Yanny, B., Newberg, H. J., Grebel, E. K., et al. 2003, *ApJ*, **588**, 824